Comput Mech (2013) 51:1061–1073
DOI 10.1007/s00466-012-0790-y

ORIGINAL PAPER

Patient-specific computational analysis of the influence of a stent on the unsteady flow in cerebral aneurysms

Kenji Takizawa · Kathleen Schjodt · Anthony Puntel · Nikolay Kostov · Tayfun E. Tezduyar

Received: 23 July 2012 / Accepted: 28 August 2012 / Published online: 21 September 2012

Abstract We present a patient-specific computational analysis of the influence of a stent on the unsteady flow in cerebral aneurysms. The analysis is based on four different arterial models extracted form medical images, and the stent is placed across the neck of the aneurysm to reduce the flow circulation in the aneurysm. The core computational technique used in the analysis is the space–time (ST) version of the variational multiscale (VMS) method and is called "DSD/SST-VMST". The special techniques developed for this class of cardiovascular fluid mechanics computations are used in conjunction with the DSD/SST-VMST technique. The special techniques include NURBS representation of the surface over which the stent model and mesh are built, mesh generation with a reasonable resolution across the width of the stent wire and with refined layers of mesh near the arterial and stent surfaces, modeling the double-stent case, and quantitative assessment of the flow circulation in the aneurysm. We provide a brief overview of the special techniques, compute the unsteady flow patterns in the aneurysm for the four arterial models, and investigate in each case how those patterns are influenced by the presence of single and double stents.

K. Takizawa
Department of Modern Mechanical Engineering, Waseda Institute for Advanced Study, Waseda University, 1-6-1 Nishi-Waseda, Shinjuku-ku, Tokyo 169-8050 Japan

K. Schjodt · A. Puntel · N. Kostov · T. E. Tezduyar (✉)
Mechanical Engineering, Rice University, MS 321, 6100 Main Street, Houston, TX, 77005 USA
e-mail: tezduyar@rice.edu

Keywords Cardiovascular fluid mechanics · Patient-specific modeling · Cerebral aneurysms · Stent · Double stent · Mesh generation

1 Introduction

Computational cardiovascular fluid mechanics has been one of the most popular research areas in computational mechanics (see, for example, [1–39]). Addressing the computational challenges involved in fluid–structure interaction (FSI) between the blood flow and cardiovascular wall, which of course makes the computations more realistic, has been one of the main reasons for the rapid expansion of this research area. Many of the articles cited above are on patient-specific modeling of arteries, especially cerebral arteries with aneurysm. Patient-specific analysis of the unsteady flow in cerebral aneurysms with a stent also involves computational challenges, mostly related to the need to have a good spatial representation of the stent, with a reasonable mesh resolution across the width of the stent wire and in the normal direction near the arterial and stent surfaces. In this article we address those challenges and present a computational analysis based on four different arterial models, where we assess the influence of the stent on the flow circulation in the aneurysm. For each model, we investigate both the singe- and double-stent cases. Including the FSI in the modeling would make the computations even more realistic, and more challenging, but at this stage of our work we hold the arteries rigid, since our main objective is to evaluate the influence of the stent. We believe this objective can be reached to a certain extent without taking the FSI into account.

In the computation reported here, as the core method we use the deforming-spatial-domain/stabilized space–time (DSD/SST) formulation [40–46], which is a moving-mesh

technique. It is an alternative to the arbitrary Lagrangian–Eulerian (ALE) finite element formulation [47], which is still the most popular moving-mesh technique used in computational cardiovascular fluid mechanics. The DSD/SST method, however, has also been one of the most widely used techniques in patient-specific arterial FSI computations reported in the literature (see [1–3,6,5–7,9,10,14,15,18–22,31,33,34,37–39]), with almost all of the computations focusing on cerebral arteries with aneurysm. The DSD/SST method, like many ALE methods, is based on the streamline-upwind/Petrov-Galerkin (SUPG) [48] and pressure-stabilizing/Petrov-Galerkin [40,49] stabilizations. The specific version of the DSD/SST method we use in the computations is the space–time (ST) version [45,46] of the residual-based variational multiscale (VMS) method [50–53]. It was named "DSD/SST-VMST" (i.e. the version with the VMS turbulence model) in [45], which is also called "ST-VMS" (meaning "Space–Time VMS") in [46]. It has been successfully tested on wind-turbine rotor aerodynamics in [54,55], simple FSI problems in [46], and aerodynamics of flapping wings in [56–58]. Although we do not need a moving-mesh method in our computations here, we still use the DSD/SST method. As pointed out in [45,46,59], the DSD/SST method, because of its space-time nature, has several desirable features.

A number of special techniques for arterial fluid mechanics were developed to be used in conjunction with the DSD/SST technique. The special techniques used in the computations here include techniques for calculating an estimated zero-pressure (EZP) arterial geometry [9,18,20,34,37,60,61], a special mapping technique for specifying the velocity profile at an inflow boundary with non-circular shape [18,61], techniques for using variable arterial wall thickness [18,20,61], mesh generation techniques for building layers of refined fluid mechanics mesh near the arterial walls [14,18,20,61], techniques [20] for calculation of the wall shear stress and oscillatory shear index (OSI), techniques [31] for extracting the arterial-lumen geometry from 3D rotational angiography (3DRA) and generating a mesh for that geometry, and a new scaling technique [34,37] for specifying a more realistic volumetric flow rate.

Additional special techniques have been developed in [39] to address the challenges specific to computation of flows in cerebral arteries with aneurysm and stent. They include NURBS [62,63] representation of the surface over which the stent model and mesh are built, mesh generation with a reasonable resolution across the width of the stent wire and with refined layers of mesh near the arterial and stent surfaces, modeling the double-stent case, and quantitative assessment of the flow circulation in the aneurysm. The arterial-lumen geometries were extracted from the 3DRA images that were provided to us while carrying out the arterial FSI research reported in [31,34,37]. In the computations, we use the lumen geometries obtained after the artery goes through the EZP process [34,37] and is inflated to a pressure corresponding to the pressure at the start of our computation cycle (cardiac cycle), which is approximately 80 mm Hg. We do that instead of directly using the geometries extracted from the 3DRA so that we have a consistent basis for comparison with future FSI computations with these lumen geometries.

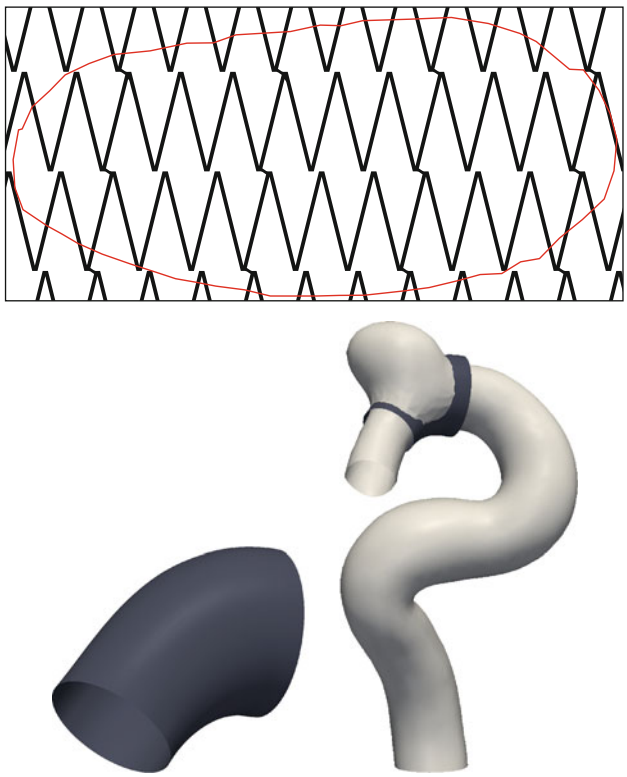

Fig. 1 Flat stent (*top*), stent mapped to a NURBS surface (*bottom left*), and lumen split with the stent (*bottom right*). The closed *curve* marked on the flat stent is the intersection of the NURBS surface and lumen and serves as the periphery of the interior boundary containing the stent

In Sect. 2 we provide an overview of the model and mesh generation process. The computational results are presented in Sect. 3, and the concluding remarks are given in Sect. 4.

2 Model and mesh generation

Model and mesh generation for a cerebral artery with aneurysm and stent requires numerous steps, and the details are provided in [39]. Here we provide a summary of the process. We start with the flat stent and the arterial lumen, and map the stent to a NURBS surface, which fits across the neck of the aneurysm (see Fig. 1).

The flat-stent model was generated using the geometry of a Cordis Precise Pro Rx nitinol self-expanding stent

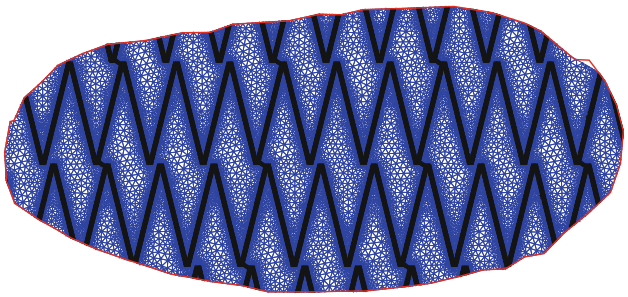

Fig. 2 Stent mesh

(PC0630RXC) with a wire diameter of about 0.1 mm. The arterial surface was extracted from medical images and a lumen reflective of the inflated arterial-wall structure was generated through the process reported in [31]. The intersection of the NURBS surface and lumen serves as the periphery of the interior boundary containing the stent, and we model and mesh only that part of the stent as shown in Fig. 2. The width of the stent wire is meshed with three to four elements (see [39] for details). The periphery of the interior-boundary mesh splits the lumen geometry into parent and aneurysm segments. For the zero-thickness representation of the stent, which is the case for the computations presented in this paper, the interior-boundary mesh serves as the surface mesh for the volume meshes generated over the parent and aneurysm parts of the arterial volume. Using also the surface meshes for the parent and aneurysm segments of the lumen, we generate layers of refined mesh on either side of the stent and near the arterial walls. We use four layers, each increasing in thickness with a progression ratio of 1.75 (the same number of layers and progression ratio used in [31]). The details of the thickness calculations, which include the solution of the Laplace's equation over the surfaces to calculate the variable thickness of the first layer, can be found in [31,39]. The rest of the fluid volume mesh is generated by using the innermost surface of the layers of refined mesh as the surface mesh for generating the volume mesh in both the parent and aneurysm parts of the arterial volume.

Remark 1 We generate the double stent by overlaying two single flat-stent geometries and translating one of them in two directions. We map the intersection of the deformed NURBS surface and lumen geometry, which is again the periphery of the interior boundary, to the flat double-stent geometry and mesh the double stent as one mesh. The double-stent mesh is treated the same as the single-stent mesh in the remaining mesh generation steps. Figure 3 shows the full single and double stents.

Remark 2 The mesh generation process for the finite-thickness representation can be found in [39], together with comparative computations for the zero- and finite-thickness representations.

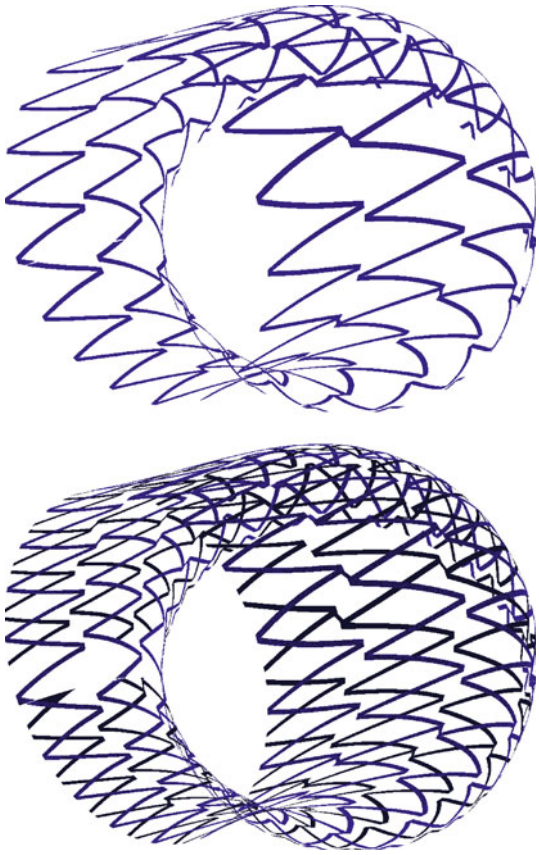

Fig. 3 Surface for single (*top*) and double (*bottom*) stents

3 Computational results

3.1 Computational models

As it was done for the computations reported in [1–3,6,7], the blood is assumed to behave like a Newtonian fluid (see Sect. 2.1 in [9]). The density and kinematic viscosity are set to 1,000 kg/m^3 and 4.0×10^{-6} m^2/s. Other computational conditions, including the structural properties used in the EZP and inflation processes and the boundary conditions used in the flow computations can be found in [34].

Four patient-specific cerebral arteries with aneurysm are studied at three states: before stenting, after stenting with a

Table 1 Physical parameters for the four arterial models

Model	D_{I}	D_{O1}	D_{O2}	α	$Q_{\max}$
Model 1	3.7	2.9		2.33	2.05
Model 2	2.8	2.4	2.7	1.75	0.78
Model 3	4.4	2.6		2.73	3.40
Model 4	3.5	1.7	2.1	2.21	1.63

Diameters are in mm and peak volumetric flow rate is in ml/s. Here D_{I}, D_{O1}, and D_{O2} are the diameters at the inflow, first outflow, and second outflow, respectively. Also, α and $Q_{\max}$ are Womersley number and peak volumetric flow rate, respectively

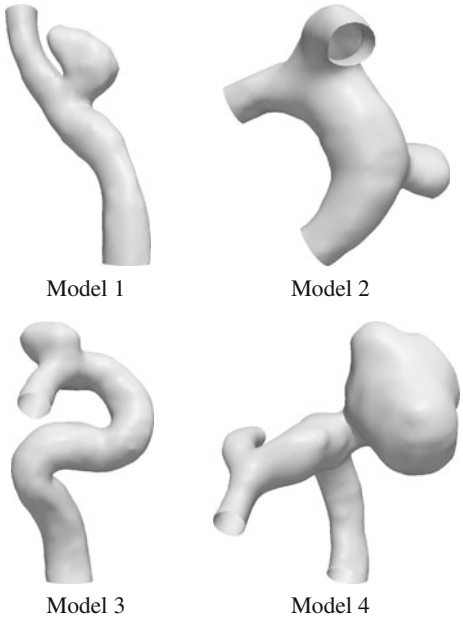

Fig. 4 Arterial lumen geometry obtained from voxel data for the four models studied

single stent, and after stenting with two stents. The physical parameters for the four arterial models are listed in Table 1 and the lumen geometries are shown in Fig. 4. The fluid mechanics meshes for the single-stent case for the four models are shown in Figs. 5, 6, 7, 8. The cross-section view shows the refined mesh at the aneurysm neck on either side of the boundary separating the aneurysm from the parent artery. The node and element numbers for the 12 fluid mechanics meshes are given in Table 2.

All computations are carried out using the DSD/SST-VMST technique (see [45,46] for the terminology), with the stabilization parameters as given by Eqs. (7)–(11) in [44] for $\tau_{\mathrm{M}} = \tau_{\mathrm{SUPG}}$ and Eq. (37) in [56] for ν_{C}. The time step size is 3.333×10^{-3} s. The number of nonlinear iterations per time step is 4 and the number of GMRES iterations per nonlinear iteration for each model are shown in Table 3. We check the mass balance as one of the indicators of numerical convergence, and set the number of GMRES iterations accordingly. Sufficient mass balance is reached when the difference between the inflow and outflow rates essentially equals zero. Figures showing the mass balance for Model 1 can be found in [39].

3.2 Comparative study

The stent free area at the neck of the aneurysm is reduced to approximately 85 and 71 % in the single- and double-stent cases for all four models, respectively. We compare the fluid mechanics before and after stenting in each of the four models by analyzing the ratio of the aneurysm-inflow rate to the

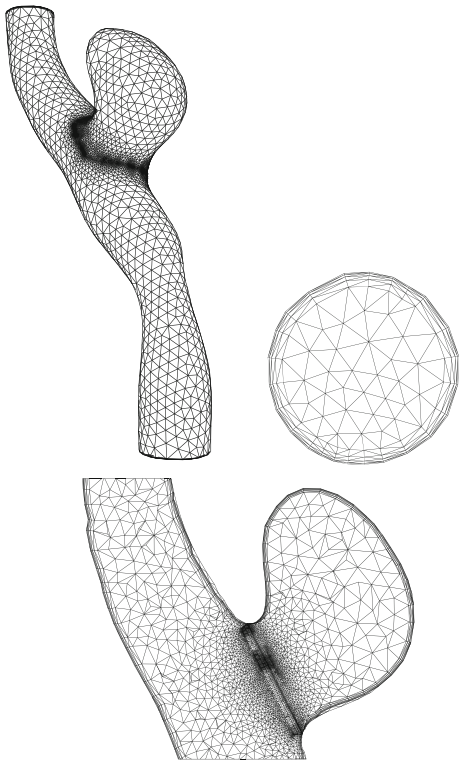

Fig. 5 Model 1. Fluid mechanics mesh for the single-stent case, with cross-section and inflow plane views

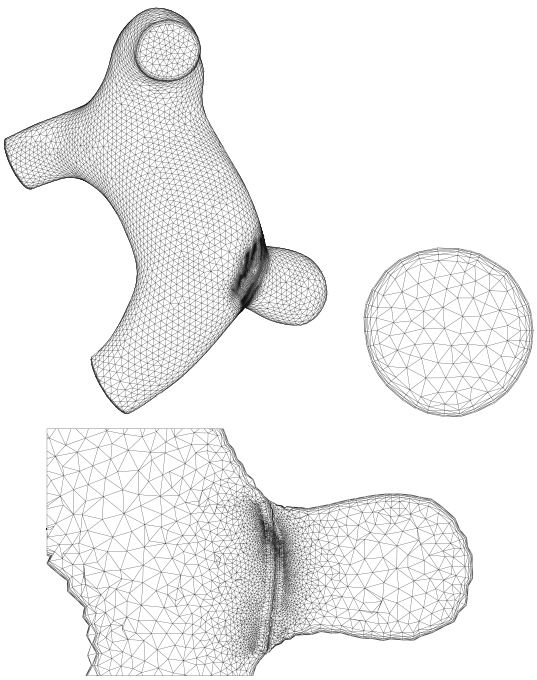

Fig. 6 Model 2. Fluid mechanics mesh for the single-stent case, with cross-section and inflow plane views

time-averaged parent-artery-inflow rate $\frac{Q_{\mathrm{A}}}{Q_{\mathrm{P}}}$, the spatially averaged kinetic energy and vorticity in the aneurysm, and OSI. The aneurysm-inflow rate is calculated by integrating

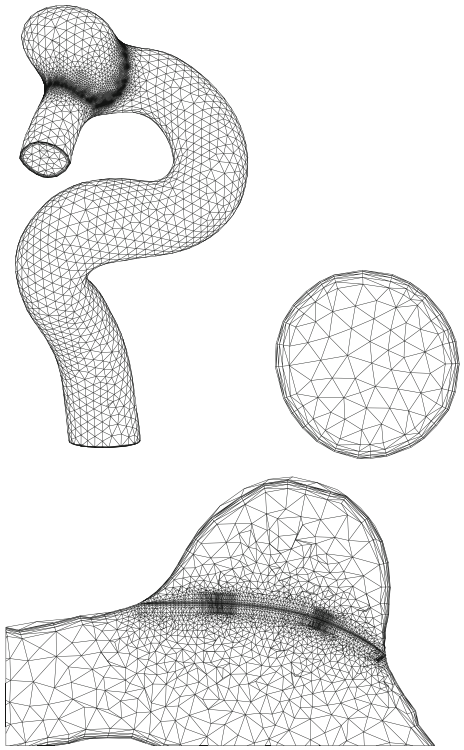

Fig. 7 Model 3. Fluid mechanics mesh for the single-stent case, with cross-section and inflow plane views

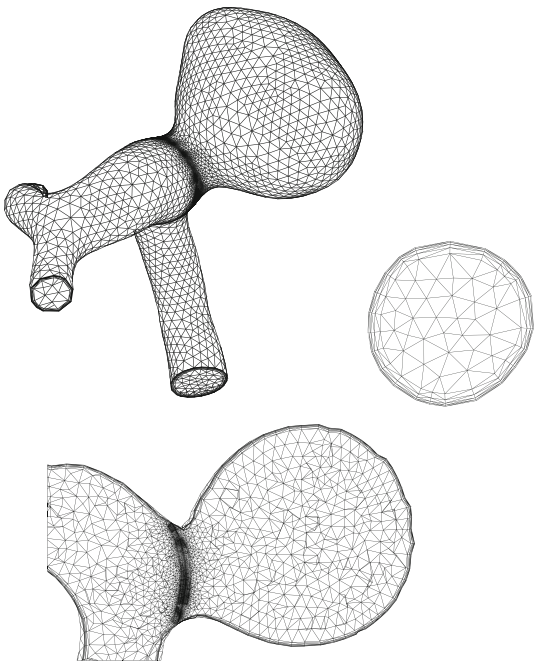

Fig. 8 Model 4. Fluid mechanics mesh for the single-stent case, with cross-section and inflow plane views

the magnitude of the normal component of the velocity over the interior-boundary mesh containing the stent and dividing that by 2. We divide by 2, because the integral of the magnitude of the normal component of the velocity measures twice

Table 2 Number of nodes and elements for the fluid mechanics mesh for each case of the four models

	Model 1		Model 2	
	nn	*ne*	*nn*	*ne*
No	527,323	3,168,305	430,497	2,532,798
Single	566,049	3,300,182	442,454	2,532,798
Double	662,431	3,736,603	503,819	2,823,729
	Model 3		Model 4	
	nn	*ne*	*nn*	*ne*
No	530,268	3,136,903	428,260	2,522,129
Single	552,922	3,136,903	447,430	2,522,129
Double	930,403	5,261,467	867,500	4,916,931

Here *nn* and *ne* are number of nodes and elements, respectively

Table 3 GMRES iterations per nonlinear iteration for each case of the four arterial models

	Model 1	Model 2	Model 3	Model 4
No	1,000	1,000	1,500	1,000
Single	1,500	1,000	1,500	1,000
Double	1,500	1,200	2,000	1,700

the inflow rate. The effectiveness of stenting using either the single or double stent depends on the degree to which the flow characteristics were altered and also the arterial geometry and size of the aneurysm. The higher OSI observed in stent cases for all models follows the belief that regions with increased OSI prompt thrombus formation [64,65].

3.2.1 Model 1

The aneurysm in Model 1 has a volume of 0.10 cm^3 and approximate neck area of 0.47 cm^2. The total area in the neck blocked by the stent in the single- and double-stent cases is 0.07 and 0.13 cm^2, respectively. Figures 9, 10, 11, 12 show the reduction in blood flow into and within the aneurysm caused by stenting. The parent artery has an average inflow rate of 0.62 ml/s. The peak blood flow into and within the aneurysm occurs approximately 0.02 s before peak inflow rate in the parent artery. The time-averaged $\frac{Q_A}{Q_P}$ decreases by 22 and 78 % in the single- and double-stent cases, respectively. Similarly, the kinetic energy averaged in space and time decreases by 72 % in the single-stent case and 92 % in the double-stent case. The reduction in vorticity in the aneurysm caused by stenting is shown in Figs. 13 and 14. The vorticity, averaged in space and time, is reduced by 47 and 72 % in the single- and double-stent cases, respectively. Figure 15 shows the OSI for all three cases.

3.2.2 Model 2

The aneurysm in Model 2 is the smallest of the four models, computed with a volume of 0.04 cm^3 and approximate

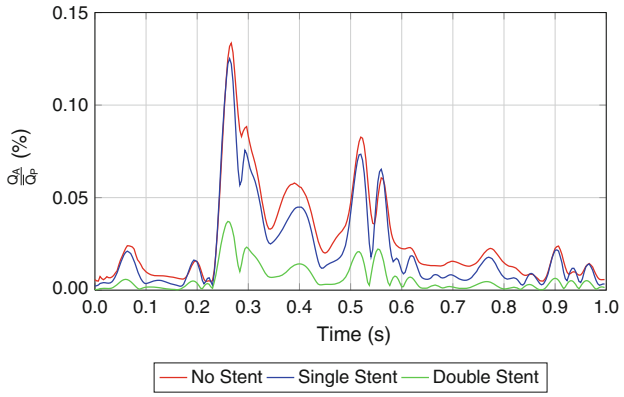

Fig. 9 Model 1. Comparison of $\frac{Q_A}{Q_P}$ for the three cases

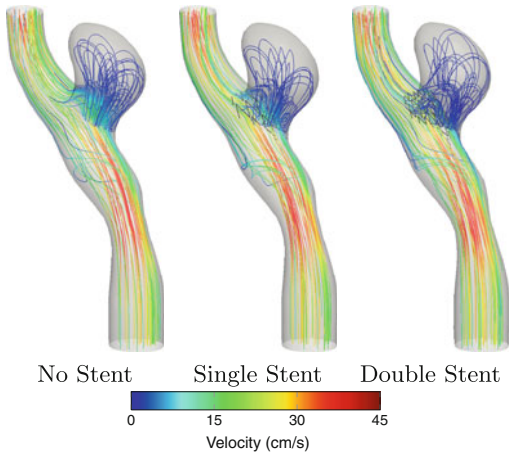

Fig. 10 Model 1. Streamlines showing changes in blood flow patterns and velocity induced by stenting at peak flow into the parent artery

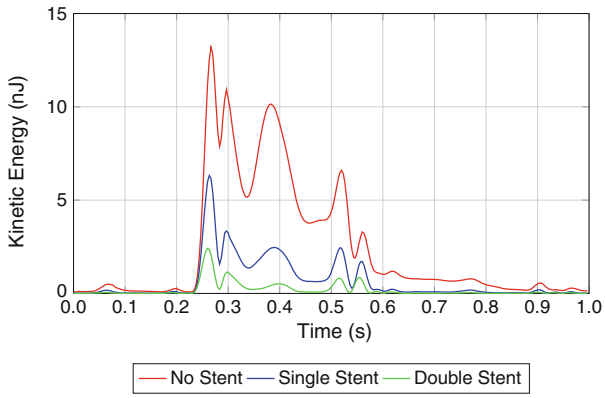

Fig. 11 Model 1. Comparison of spatially averaged kinetic energy in the aneurysm

neck area of 0.36 cm^2. The stent area for the single- and double-stent cases are 0.05 and 0.10 cm^2, respectively. The average inflow rate for Model 2 is significantly lower than the other three models at 0.26 ml/s. The change in blood flow velocity is shown in Figs. 16, 17, 18, 19. Peak blood flow into the aneurysm, along with peak kinetic energy, occurs approximately 0.13 s after peak inflow rate into the parent artery. In Fig. 16, the time-averaged flow-rate ratio is reduced by 41 % in the single-stent case and 81 % in the double-stent case. As can be seen in Fig. 18, the kinetic energy within the stent is significantly reduced with the single stent alone. The kinetic energy within the aneurysm averaged in space and time decreases by 83 and 95 % in the single- and double-stent cases, respectively. The change in vorticity between the three cases is shown in Figs. 20 and 21. The single-stent case exhibits a 50 % reduction in vorticity averaged in space and time while the double-stent case shows a 69 % reduction.

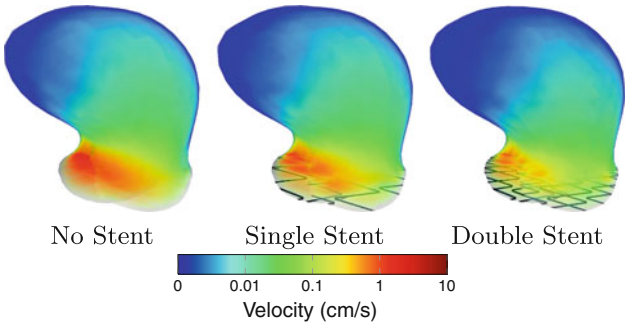

Fig. 12 Model 1. Volume rendering of aneurysm velocity magnitude at peak flow into the aneurysm

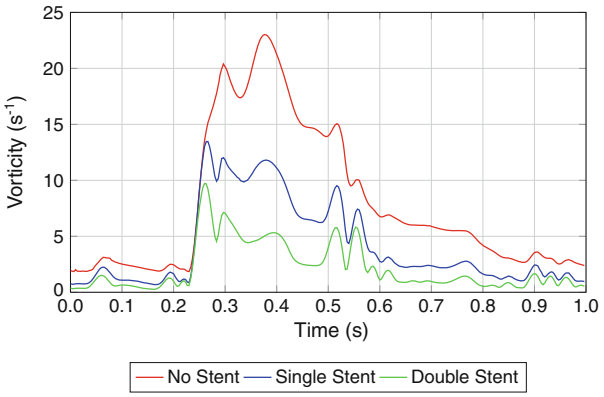

Fig. 13 Model 1. Comparison of spatially averaged vorticity magnitude in the aneurysm

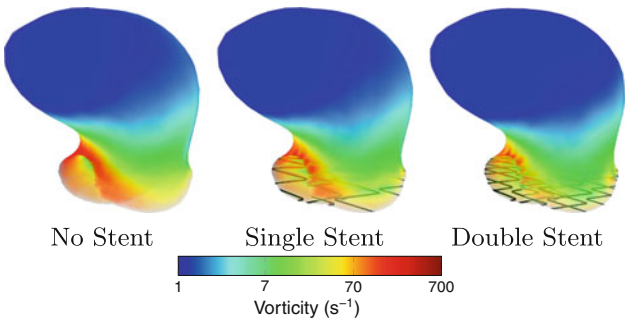

Fig. 14 Model 1. Volume rendering of aneurysm vorticity magnitude at peak flow into the aneurysm

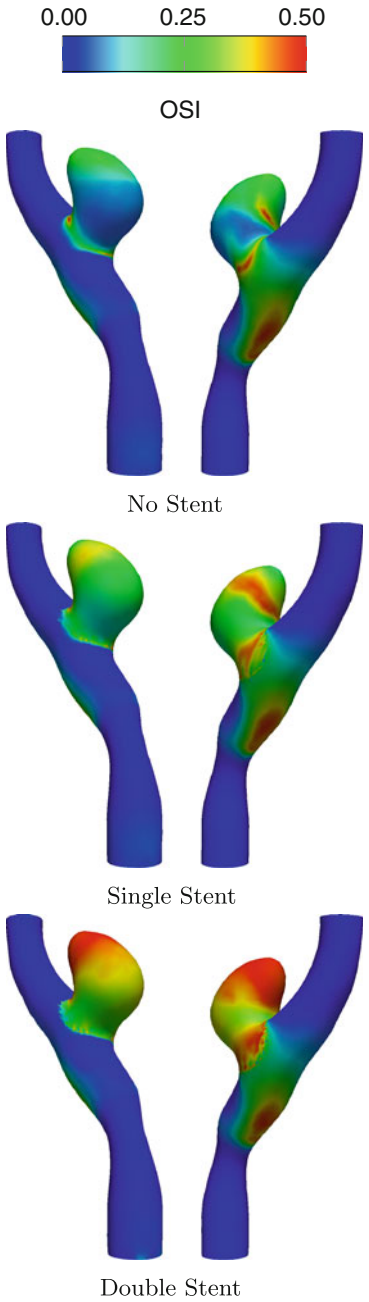

Fig. 15 OSI for Model 1

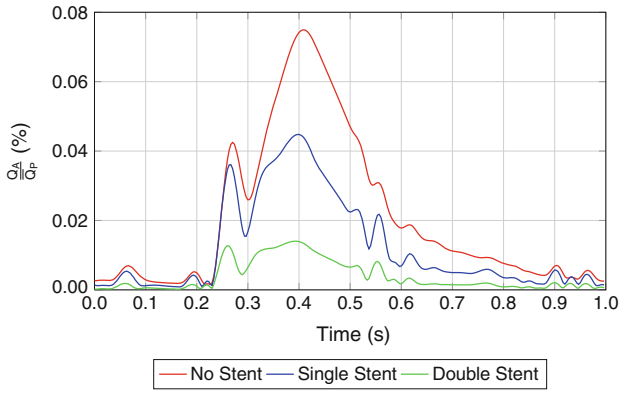

Fig. 16 Model 2. Comparison of $\frac{Q_A}{Q_P}$ for the three cases

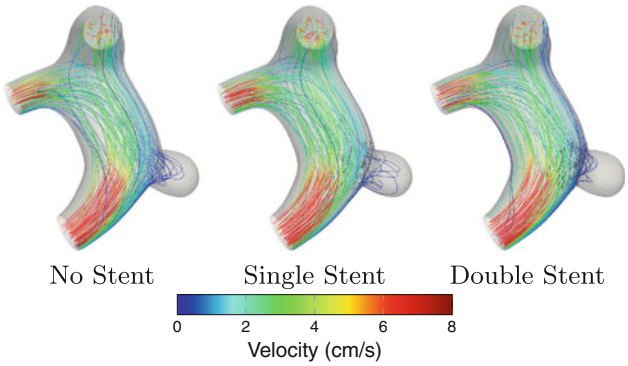

Fig. 17 Model 2. Streamlines showing changes in blood flow patterns and velocity induced by stenting at peak flow in the parent artery

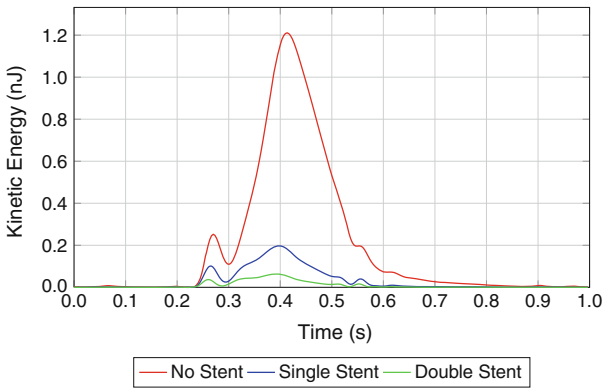

Fig. 18 Model 2. Comparison of spatially averaged kinetic energy in the aneurysm

Figure 22 shows the increase in OSI from before stenting to stenting with two stents.

3.2.3 Model 3

The geometry of Model 3 has a pronounced curvature just prior to and at the aneurysm location. The small size of the aneurysm, 0.05 cm^3 in volume, coupled with the significant curvature, results in greater blood flow into and within the aneurysm compared to the other models. The neck of the aneurysm spans an area of 0.60 cm^2, the largest neck area of the four models, contrary to the overall small size of the aneurysm. The single stent covers an area of 0.09 cm^2 and the double stent nearly doubles the area covered to 0.17 cm^2. Figures 23, 24, 25, 26 show the changes induced by deploying a stent to treat the aneurysm. The average inflow rate for the parent artery is slightly higher than the other models at 0.97 ml/s. The peak flow into the aneurysm occurs approximately 0.02 s after peak

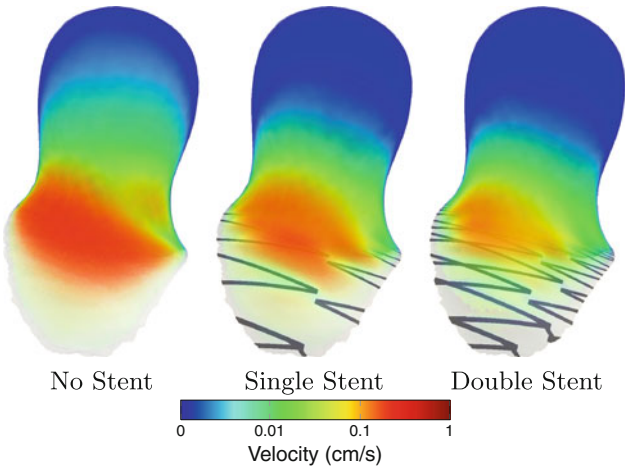

Fig. 19 Model 2. Volume rendering of aneurysm velocity magnitude at peak flow into the aneurysm

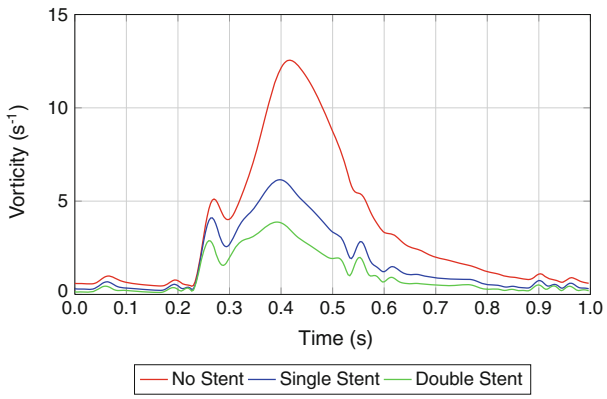

Fig. 20 Model 2. Comparison of spatially averaged vorticity magnitude in the aneurysm

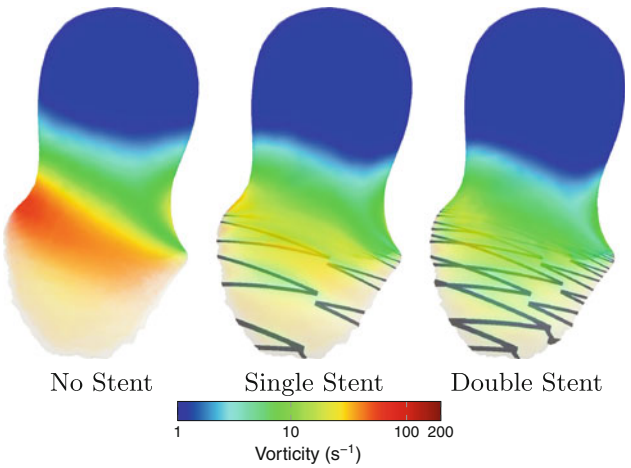

Fig. 21 Model 2. Volume rendering of aneurysm vorticity magnitude at peak flow into the aneurysm

flow into the parent artery. On average, $\frac{Q_A}{Q_P}$ decreases by 16 and 78 % in the single- and double-stent cases, respectively. The single-stent case has a significant drop in average

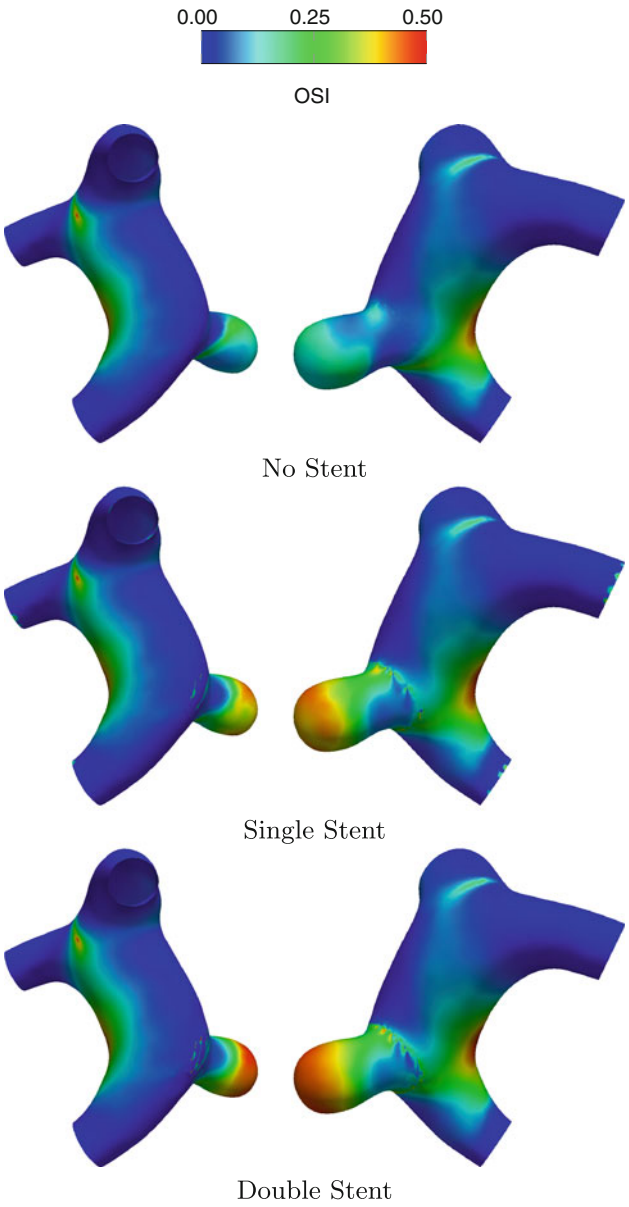

Fig. 22 OSI for Model 2

kinetic energy at 66 % and the double-stent case is reduced about 87 %. The vorticity in the aneurysm follows a similar pattern to kinetic energy and the reduction is shown in Figs. 27 and 28. The average vorticity decreases 41 and 62 % in the single- and double-stent cases, respectively. Figure 29 shows the OSI for all three cases.

3.2.4 Model 4

Model 4 has the largest aneurysm of the four arteries studied with a volume of 0.61 cm^3 and has the second largest neck with an area spanning 0.53 cm^2. The single and double stents cover an area of 0.08 and 0.15 cm^2, respectively. For the

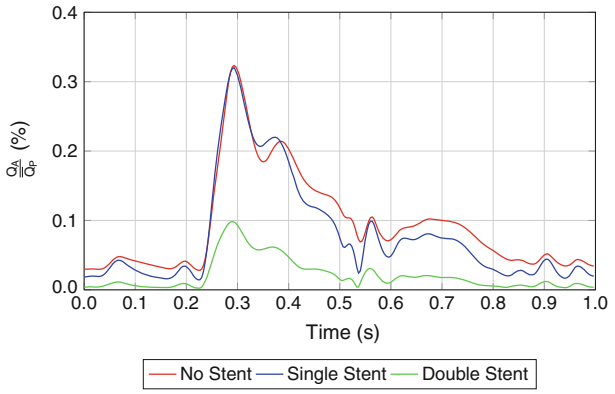

Fig. 23 Model 3. Comparison of $\frac{Q_A}{Q_P}$ for the three cases

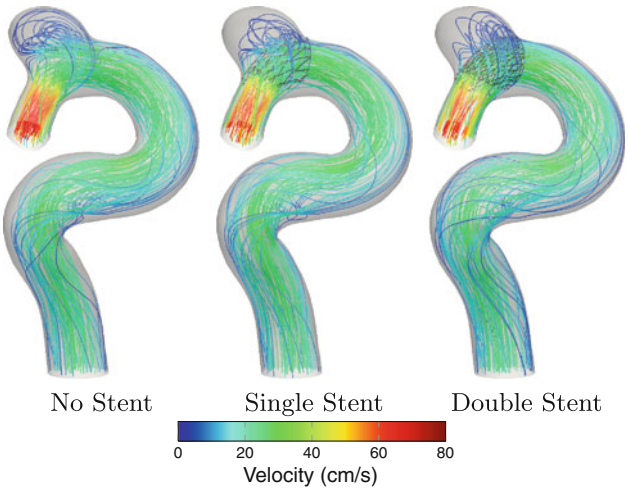

Fig. 24 Model 3. Streamlines showing changes in blood flow patterns and velocity induced by stenting at peak flow in the parent artery

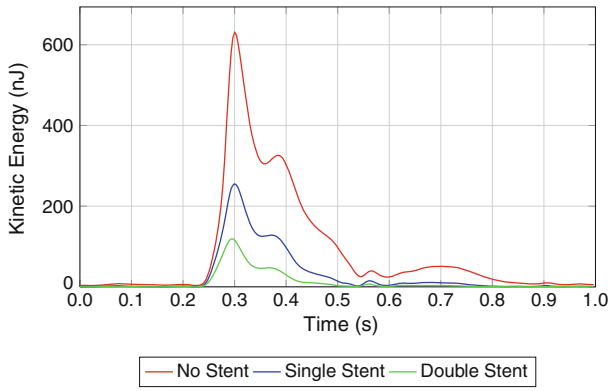

Fig. 25 Model 3. Comparison of spatially averaged kinetic energy in the aneurysm

no-stent case, we report the results from the computation of the second cardiac cycle, because the first cycle is not enough to obtain temporally periodic values for the quantities displayed. A gradual decrease in flow going into the aneurysm is observed from the no-stent case to the double-stent case. The single-stent case has a reduction of 37 % in $\frac{Q_A}{Q_P}$

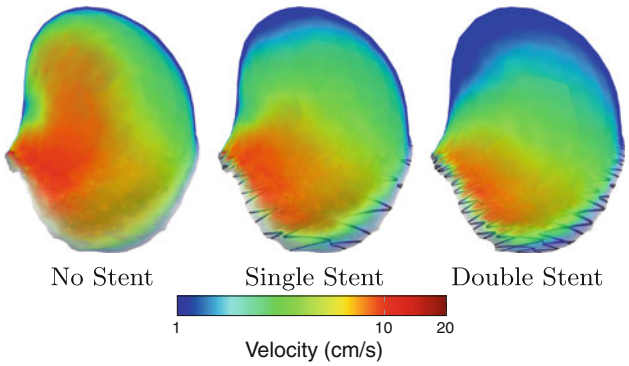

Fig. 26 Model 3. Volume rendering of aneurysm velocity magnitude at peak flow into the aneurysm

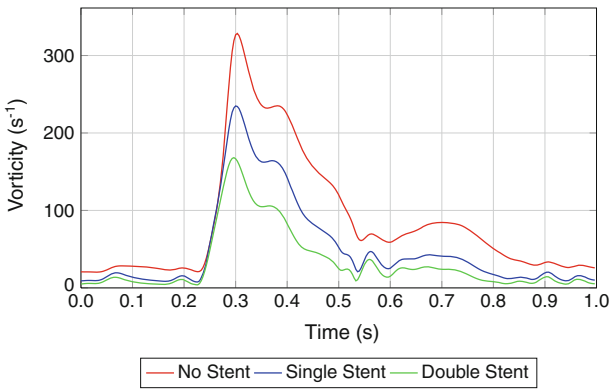

Fig. 27 Model 3. Comparison of spatially averaged vorticity magnitude in the aneurysm

and the double-stent case has a 82 % reduction. A dramatic reduction in kinetic energy occurs in both of the stent cases compared to the no-stent case, with 89 % decrease in the single-stent case and 97 % in the double-stent case. Figures 30, 31, 32, 33 show the reduction in blood flow. The average inflow rate into the parent artery is 0.50 ml/s and the peak blood flow into the aneurysm occurs 0.04 s after peak inflow rate into the parent artery. Similarly to kinetic energy, vorticity drops significantly in the stented cases as shown in Figs. 34 and 35. The average reduction for the single-stent case is 72 % and for the double-stent case 86 %. The OSI for all three cases is shown in Fig. 36.

4 Concluding remarks

We addressed the challenges involved in patient-specific computation of the unsteady flow in cerebral aneurysms with a stent and presented an analysis of the influence of the stent on the flow circulation in the aneurysm. We used in the analysis four different arterial models extracted form medical images, and placed the stent across the neck of the aneurysm to reduce the flow circulation. For each model, we computed

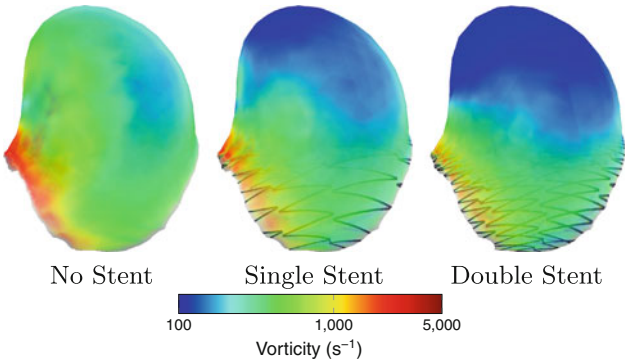

Fig. 28 Model 3. Volume rendering of aneurysm vorticity magnitude at peak flow into the aneurysm

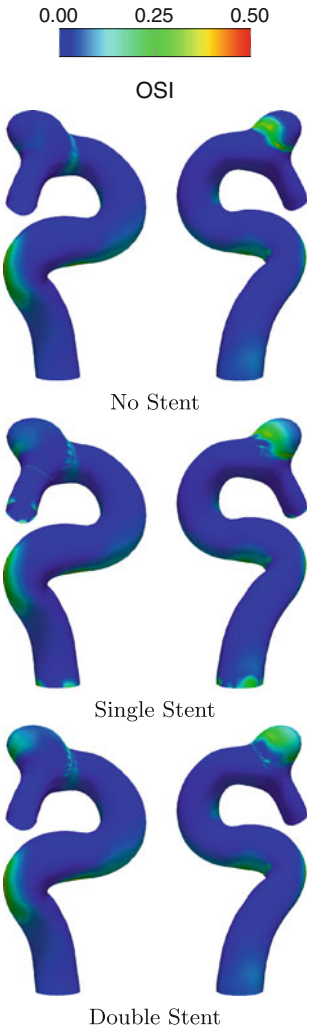

Fig. 29 OSI for Model 3

both the singe- and double-stent cases, and also the no-stent case. As the core method we used the DSD/SST method, which, because of its space-time nature, has several desirable features. The specific version of the DSD/SST method we used is the DSD/SST-VMST, which is the space-time version of the residual-based VMS method. A good number

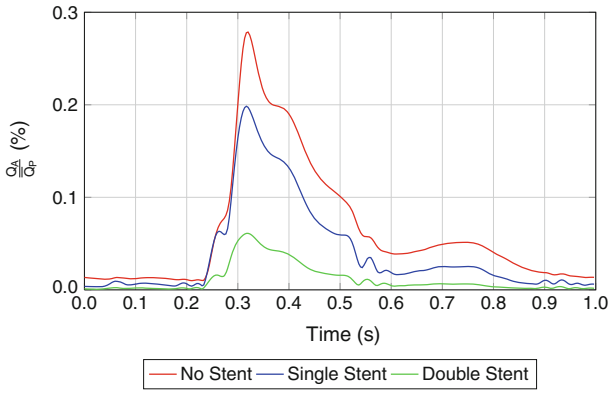

Fig. 30 Model 4. Comparison of $\frac{Q_A}{Q_P}$ for the three cases

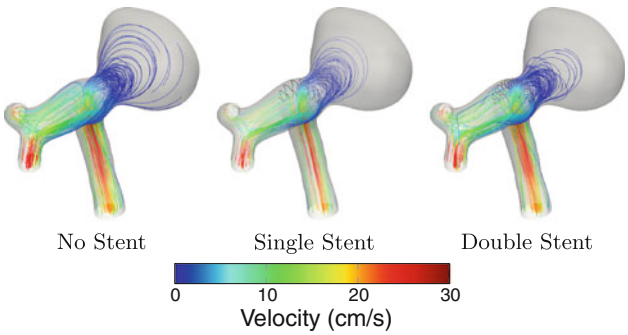

Fig. 31 Model 4. Streamlines showing changes in blood flow patterns and velocity induced by stenting at peak flow in the parent artery

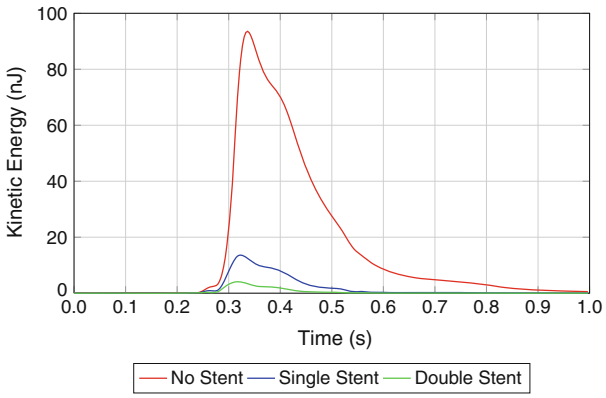

Fig. 32 Model 4. Comparison of spatially averaged kinetic energy in the aneurysm

of special techniques targeting arterial fluid mechanics computations were also used in conjunction with the DSD/SST-VMST method. Furthermore, we used some additional special techniques developed to address the challenges specific to computation of flows in cerebral arteries with aneurysm and stent. The additional techniques include NURBS representation of the surface over which the stent model and mesh are built, mesh generation with a reasonable resolution across the width of the stent wire and with refined layers of mesh

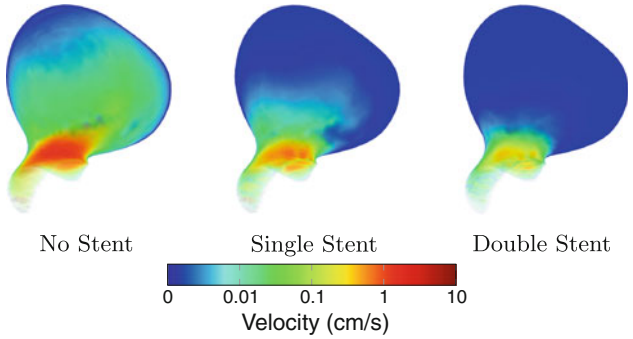

Fig. 33 Model 4. Volume rendering of aneurysm velocity magnitude at peak flow into the aneurysm

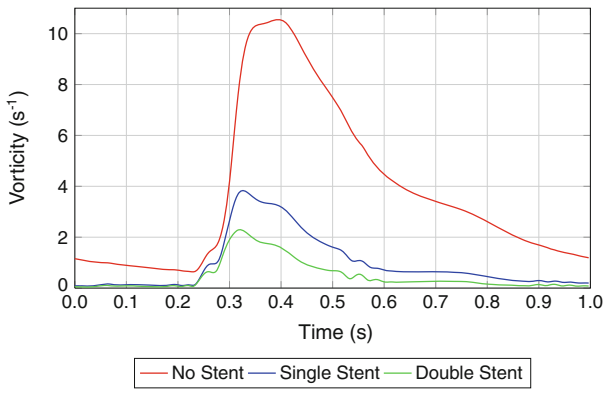

Fig. 34 Model 4. Comparison of spatially averaged vorticity magnitude in the aneurysm

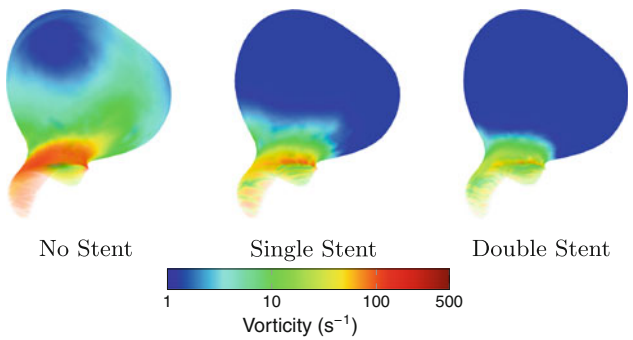

Fig. 35 Model 4. Volume rendering of aneurysm vorticity magnitude at peak flow into the aneurysm

near the arterial and stent surfaces, modeling the double-stent case, and quantitative assessment of the flow circulation in the aneurysm. With a total of 12 computations for the four models, we presented an extensive evaluation of the influence of placing a stent across the neck of the aneurysm. We quantified the evaluation in terms of the ratio of the aneurysm-inflow rate to the time-averaged parent-artery-inflow rate, the spatially averaged kinetic energy and vorticity in the aneurysm, and OSI. We observed significant decreases in the first three of these quantitative measures with a single stent, and even

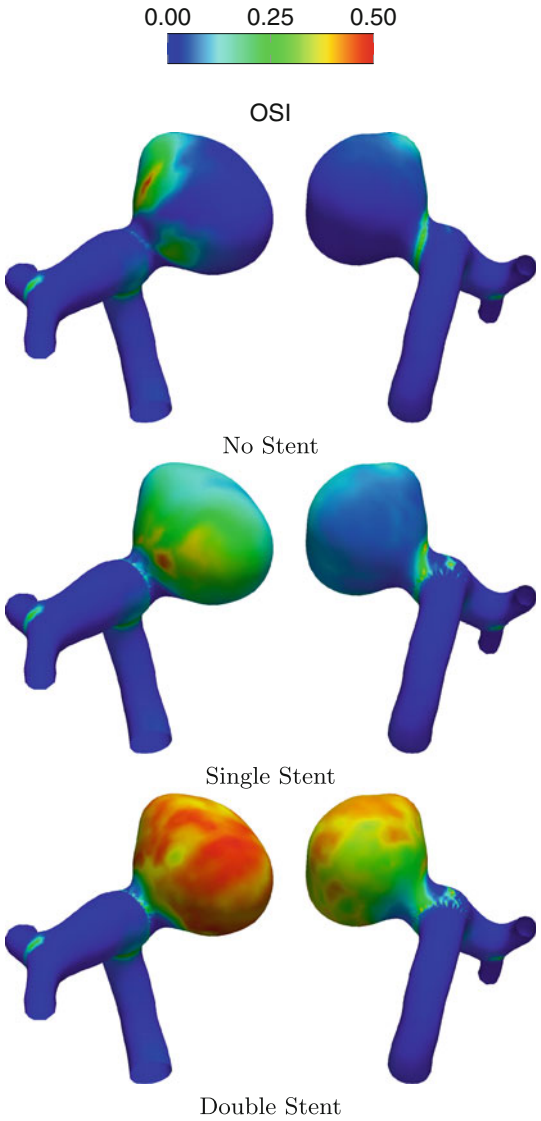

Fig. 36 OSI for Model 4

more with a double stent. The computations show that the core and special techniques constitute a powerful tool for analysis of how well a stent performs in reducing the flow circulation in a cerebral aneurysm, and this can be used is design studies for such stents.

Acknowledgment This work was supported in part by a seed Grant from the Gulf Coast Center for Computational Cancer Research funded by John and Ann Doerr Fund for Computational Biomedicine. It was also supported in part by the Program to Disseminate Tenure Tracking System, Ministry of Education, Culture, Sports, Science and Technology, Japan. Supercomputing resources were provided in part by the Rice Computational Research Cluster funded by NSF Grant CNS-0821727. We thank Dr. Ryo Torii (University College London) for the inflow velocity waveform used in the computations. Dr. Peng R. Chen (University of Texas Medical School at Houston) provided the stent sample and the arterial images from 3DRA.

References

1. Torii R, Oshima M, Kobayashi T, Takagi K, Tezduyar TE (2004) Influence of wall elasticity on image-based blood flow simulation. Jpn Soc Mech Eng J A 70:1224–1231 (in Japanese)
2. Torii R, Oshima M, Kobayashi T, Takagi K, Tezduyar TE (2006) Computer modeling of cardiovascular fluid–structure interactions with the Deforming-Spatial-Domain/Stabilized Space–Time formulation. Comput Methods Appl Mech Eng 195: 1885–1895. doi:10.1016/j.cma.2005.05.050
3. Torii R, Oshima M, Kobayashi T, Takagi K, Tezduyar TE (2006) Fluid–structure interaction modeling of aneurysmal conditions with high and normal blood pressures. Comput Mech 38: 482–490. doi:10.1007/s00466-006-0065-6
4. Bazilevs Y, Calo VM, Zhang Y, Hughes TJR (2006) Isogeometric fluid–structure interaction analysis with applications to arterial blood flow. Comput Mech 38:310–322
5. Tezduyar TE, Sathe S, Cragin T, Nanna B, Conklin BS, Pausewang J, Schwaab M (2007) Modeling of fluid–structure interactions with the space–time finite elements: arterial fluid mechanics. Int J Numer Methods Fluids 54: 901–922. doi:10.1002/fld.1443
6. Torii R, Oshima M, Kobayashi T, Takagi K, Tezduyar TE (2007) Influence of wall elasticity in patient-specific hemodynamic simulations. Comput Fluids 36: 160–168. doi:10.1016/j.compfluid.2005.07.014
7. Torii R, Oshima M, Kobayashi T, Takagi K, Tezduyar TE (2007) Numerical investigation of the effect of hypertensive blood pressure on cerebral aneurysm—dependence of the effect on the aneurysm shape. Int J Numer Methods Fluids 54: 995–1009. doi:10.1002/fld.1497
8. Bazilevs Y, Calo VM, Tezduyar TE, Hughes TJR (2007) YZβ discontinuity-capturing for advection-dominated processes with application to arterial drug delivery. Int J Numer Methods Fluids 54:593–608. doi:10.1002/fld.1484
9. Tezduyar TE, Sathe S, Schwaab M, Conklin BS (2008) Arterial fluid mechanics modeling with the stabilized space–time fluid–structure interaction technique. Int J Numer Methods Fluids 57:601–629. doi:10.1002/fld.1633
10. Torii R, Oshima M, Kobayashi T, Takagi K, Tezduyar TE (2008) Fluid–structure interaction modeling of a patient-specific cerebral aneurysm: influence of structural modeling. Comput Mech 43:151–159. doi:10.1007/s00466-008-0325-8
11. Bazilevs Y, Calo VM, Hughes TJR, Zhang Y (2008) Isogeometric fluid–structure interaction: theory, algorithms, and computations. Comput Mech 43:3–37
12. Isaksen JG, Bazilevs Y, Kvamsdal T, Zhang Y, Kaspersen JH, Waterloo K, Romner B, Ingebrigtsen T (2008) Determination of wall tension in cerebral artery aneurysms by numerical simulation. Stroke 39:3172–3178
13. Maynard JP, Nithiarasu P (2008) A 1D arterial blood flow model incorporating ventricular pressure, aortic valve and regional coronary flow using the locally conservative Galerkin (LCG) method. Commun Numer Methods Eng 24:367–417
14. Tezduyar TE, Schwaab M, Sathe S (2009) Sequentially-Coupled Arterial Fluid–Structure Interaction (SCAFSI) technique. Comput Methods Appl Mech Eng 198:3524–3533. doi:10.1016/j.cma.2008.05.024
15. Torii R, Oshima M, Kobayashi T, Takagi K, Tezduyar TE (2009) Fluid–structure interaction modeling of blood flow and cerebral aneurysm: significance of artery and aneurysm shapes. Comput Methods Appl Mech Eng 198:3613–3621. doi:10.1016/j.cma.2008.08.020
16. Bazilevs Y, Gohean JR, Hughes TJR, Moser RD, Zhang Y (2009) Patient-specific isogeometric fluid–structure interaction analysis of thoracic aortic blood flow due to implantation of the Jarvik 2000 left ventricular assist device. Comput Methods Appl Mech Eng 198:3534–3550
17. Bazilevs Y, Hsu M-C, Benson D, Sankaran S, Marsden A (2009) Computational fluid–structure interaction: methods and application to a total cavopulmonary connection. Comput Mech 45:77–89
18. Takizawa K, Christopher J, Tezduyar TE, Sathe S (2010) Space–time finite element computation of arterial fluid–structure interactions with patient-specific data. Int J Numer Methods Biomed Eng 26:101–116. doi:10.1002/cnm.1241
19. Tezduyar TE, Takizawa K, Moorman C, Wright S, Christopher J (2010) Multiscale sequentially-coupled arterial FSI technique. Comput Mech 46:17–29. doi:10.1007/s00466-009-0423-2
20. Takizawa K, Moorman C, Wright S, Christopher J, Tezduyar TE (2010) Wall shear stress calculations in space–time finite element computation of arterial fluid–structure interactions. Comput Mech 46:31–41. doi:10.1007/s00466-009-0425-0
21. Torii R, Oshima M, Kobayashi T, Takagi K, Tezduyar TE (2010) Influence of wall thickness on fluid–structure interaction computations of cerebral aneurysms. Int J Numer Methods Biomed Eng 26:336–347. doi:10.1002/cnm.1289
22. Torii R, Oshima M, Kobayashi T, Takagi K, Tezduyar TE (2010) Role of 0D peripheral vasculature model in fluid–structure interaction modeling of aneurysms. Comput Mech 46:43–52. doi:10.1007/s00466-009-0439-7
23. Bazilevs Y, Hsu M-C, Zhang Y, Wang W, Liang X, Kvamsdal T, Brekken R, Isaksen J (2010) A fully-coupled fluid–structure interaction simulation of cerebral aneurysms. Comput Mech 46:3–16
24. Sugiyama K, Ii S, Takeuchi S, Takagi S, Matsumoto Y (2010) Full Eulerian simulations of biconcave neo-Hookean particles in a Poiseuille flow. Comput Mech 46:147–157
25. Bazilevs Y, Hsu M-C, Zhang Y, Wang W, Kvamsdal T, Hentschel S, Isaksen J (2010) Computational fluid–structure interaction: methods and application to cerebral aneurysms. Biomech Model Mechanobiol 9:481–498
26. Bazilevs Y, Alamo JCdel , Humphrey JD (2010) From imaging to prediction: emerging non-invasive methods in pediatric cardiology. Prog Pediatr Cardiol 30:81–89
27. Mut F, Aubry R, Lohner R, Cebral JR (2010) Fast numerical solutions of patient-specific blood flows in 3D arterial systems. Int J Numer Methods Biomed Eng 26:73–85
28. Bevan RLT, Nithiarasu P, Loon RV, Sazanov I, Luckraz H, Garnham A (2010) Application of a locally conservative Galerkin (LCG) method for modelling blood flow through a patient-specific carotid bifurcation. Int J Numer Methods Fluids. doi:10.1002/fld.2313
29. Chitra K, Sundararajan T, Vengadesan S, Nithiarasu P (2010) Non-Newtonian blood flow study in a model cavopulmonary vascular system. Int J Numer Methods Fluids. doi:10.1002/fld.2256
30. Cebral JR, Mut F, Sforza D, Lohner R, Scrivano E, Lylyk P, Putnam C (2010) Clinical application of image-based cfd for cerebral aneurysms. Int J Numer Methods Biomed Eng. doi:10.1002/cnm.1373
31. Takizawa K, Moorman C, Wright S, Purdue J, McPhail T, Chen PR, Warren J, Tezduyar TE (2011) Patient-specific arterial fluid–structure interaction modeling of cerebral aneurysms. Int J Numer Methods Fluids 65:308–323. doi:10.1002/fld.2360
32. Manguoglu M, Takizawa K, Sameh AH, Tezduyar TE (2011) Nested and parallel sparse algorithms for arterial fluid mechanics computations with boundary layer mesh refinement. Int J Numer Methods Fluids 65:135–149. doi:10.1002/fld.2415
33. Torii R, Oshima M, Kobayashi T, Takagi K, Tezduyar TE (2011) Influencing factors in image-based fluid–structure

interaction computation of cerebral aneurysms. Int J Numer Methods Fluids 65:324–340. doi:10.1002/fld.2448
34. Tezduyar TE, Takizawa K, Brummer T, Chen PR (2011) Space–time fluid–structure interaction modeling of patient-specific cerebral aneurysms. Int J Numer Methods Biomed Eng 27:1665–1710. doi:10.1002/cnm.1433
35. Hsu M-C, Bazilevs Y (2011) Blood vessel tissue prestress modeling for vascular fluid–structure interaction simulations. Finite Elem Anal Des 47:593–599
36. Manguoglu M, Takizawa K, Sameh AH, Tezduyar TE (2011) A parallel sparse algorithm targeting arterial fluid mechanics computations. Comput Mech 48:377–384. doi:10.1007/s00466-011-0619-0
37. Takizawa K, Brummer T, Tezduyar TE, Chen PR (2012) A comparative study based on patient-specific fluid–structure interaction modeling of cerebral aneurysms. J Appl Mech 79:010908. doi:10.1115/1.4005071
38. Takizawa K, Bazilevs Y, Tezduyar TE (2012) Space–time and ALE-VMS techniques for patient-specific cardiovascular fluid–structure interaction modeling. Arch Comput Methods Eng 19:171–225. doi:10.1007/s11831-012-9071-3
39. Takizawa K, Schjodt K, Puntel A, Kostov N, Tezduyar TE (2012) Patient-specific computer modeling of blood flow in cerebral arteries with aneurysm and stent. Comput Mech. doi:10.1007/s00466-012-0760-4
40. Tezduyar TE (1992) Stabilized finite element formulations for incompressible flow computations. Adv Appl Mech 28:1–44. doi:10.1016/S0065-2156(08)70153-4
41. Tezduyar TE, Behr M, Liou J (1992) A new strategy for finite element computations involving moving boundaries and interfaces—the deforming-spatial-domain/space–time procedure: I. The concept and the preliminary numerical tests. Comput Methods Appl Mech Eng 94:339–351. doi:10.1016/0045-7825(92)90059-S
42. Tezduyar TE, Behr M, Mittal S, Liou J (1992) A new strategy for finite element computations involving moving boundaries and interfaces—the deforming-spatial-domain/space–time procedure: II. Computation of free-surface flows, two-liquid flows, and flows with drifting cylinders. Comput Methods Appl Mech Eng 94:353–371. doi:10.1016/0045-7825(92)90060-W
43. Tezduyar TE (2003) Computation of moving boundaries and interfaces and stabilization parameters. Int J Numer Methods Fluids 43:555–575. doi:10.1002/fld.505
44. Tezduyar TE, Sathe S (2007) Modeling of fluid–structure interactions with the space–time finite elements: solution techniques. Int J Numer Methods Fluids 54:855–900. doi:10.1002/fld.1430
45. Takizawa K, Tezduyar TE (2011) Multiscale space–time fluid–structure interaction techniques. Comput Mech 48:247–267. doi:10.1007/s00466-011-0571-z
46. Takizawa K, Tezduyar TE (2012) Space–time fluid–structure interaction methods. Math Models Methods Appl Sci 22:1230001. doi:10.1142/S0218202512300013
47. Hughes TJR, Liu WK, Zimmermann TK (1981) Lagrangian–Eulerian finite element formulation for incompressible viscous flows. Comput Methods Appl Mech Eng 29:329–349
48. Brooks AN, Hughes TJR (1982) Streamline upwind/Petrov–Galerkin formulations for convection dominated flows with particular emphasis on the incompressible Navier–Stokes equations. Comput Methods Appl Mech Eng 32:199–259
49. Tezduyar TE, Mittal S, Ray SE, Shih R (1992) Incompressible flow computations with stabilized bilinear and linear equal-order-interpolation velocity-pressure elements. Comput Methods Appl Mech Eng 95:221–242. doi:10.1016/0045-7825(92)90141-6
50. Hughes TJR (1995) Multiscale phenomena: Green's functions, the Dirichlet-to-Neumann formulation, subgrid scale models, bubbles, and the origins of stabilized methods. Comput Methods Appl Mech Eng 127:387–401
51. Hughes TJR, Oberai AA, Mazzei L (2001) Large eddy simulation of turbulent channel flows by the variational multiscale method. Phys Fluids 13:1784–1799
52. Bazilevs Y, Calo VM, Cottrell JA, Hughes TJR, Reali A, Scovazzi G (2007) Variational multiscale residual-based turbulence modeling for large eddy simulation of incompressible flows. Comput Methods Appl Mech Eng 197:173–201
53. Bazilevs Y, Akkerman I (2010) Large eddy simulation of turbulent Taylor–Couette flow using isogeometric analysis and the residual-based variational multiscale method. J Comput Phys 229:3402–3414
54. Takizawa K, Henicke B, Tezduyar TE, Hsu M-C, Bazilevs Y (2011) Stabilized space–time computation of wind-turbine rotor aerodynamics. Comput Mech 48:333–344. doi:10.1007/s00466-011-0589-2
55. Takizawa K, Henicke B, Montes D, Tezduyar TE, Hsu M-C, Bazilevs Y (2011) Numerical-performance studies for the stabilized space–time computation of wind-turbine rotor aerodynamics. Comput Mech 48:647–657. doi:10.1007/s00466-011-0614-5
56. Takizawa K, Henicke B, Puntel A, Spielman T, Tezduyar TE (2012) Space–time computational techniques for the aerodynamics of flapping wings. J Appl Mech 79:010903. doi:10.1115/1.4005073
57. Takizawa K, Henicke B, Puntel A, Kostov N, Tezduyar TE (2012) Space–time techniques for computational aerodynamics modeling of flapping wings of an actual locust. Comput Mech. doi:10.1007/s00466-012-0759-x
58. Takizawa K, Kostov N, Puntel A, Henicke B, Tezduyar TE (2012) Space–time computational analysis of bio-inspired flapping-wing aerodynamics of a micro aerial vehicle. Comput Mech. doi:10.1007/s00466-012-0758-y
59. Takizawa K, Wright S, Moorman C, Tezduyar TE (2011) Fluid–structure interaction modeling of parachute clusters. Int J Numer Methods Fluids 65:286–307. doi:10.1002/fld.2359
60. Tezduyar TE, Cragin T, Sathe S, Nanna B (2007) FSI computations in arterial fluid mechanics with estimated zero-pressure arterial geometry. In: Onate E, Garcia J, Bergan P, Kvamsdal T (eds) Marine 2007. CIMNE, Barcelona
61. Tezduyar TE, Takizawa K, Christopher J (2009) Multiscale Sequentially-Coupled Arterial Fluid–Structure Interaction (SCAFSI) technique. In: Hartmann S, Meister A, Schaefer M, Turek S (eds.) International workshop on fluid–structure interaction—-theory, numerics and applications. Kassel University Press, Kassel, pp 231–252. ISBN 978-3-89958-666-4
62. Hughes TJR, Cottrell JA, Bazilevs Y (2005) Isogeometric analysis: CAD, finite elements, NURBS, exact geometry, and mesh refinement. Comput Methods Appl Mech Eng 194:4135–4195
63. Cottrell JA, Hughes TJR, Bazilevs Y (2009) Isogeometric analysis. Toward integration of CAD and FEA. Wiley, New York
64. Rhee K, Han MH, Cha SH, Khang G (2001) The changes of flow characteristics caused by a stent in fusiform aneurysm models, Engineering in Medicine and Biology Society, 2001. Proc 23rd Annu Int Conf IEEE 1: 86–88. doi:10.1109/IEMBS.2001.1018852
65. Jou L-D, Mawad ME (2011) Hemodynamic effect of neuroform stent on intimal hyperplasia and thrombus formation in a carotid aneurysm. Med Eng Phys 33:573–580. doi:10.1016/j.medengphy.2010.12.013